# **Nanoscale**



**PAPER** 

View Article Online



Cite this: Nanoscale, 2018, 10, 3225

# A crystalline and 3D periodically ordered mesoporous quaternary semiconductor for photocatalytic hydrogen generation†

Tobias Weller,<sup>a</sup> Leonie Deilmann,<sup>b</sup> Jana Timm,<sup>a</sup> Tobias S. Dörr, <sup>b</sup>c,<sup>d</sup>
Peter A. Beaucage, <sup>e</sup> Alexey S. Cherevan, <sup>b</sup>Ulrich B. Wiesner,<sup>e</sup> Dominik Eder <sup>b</sup>and Roland Marschall <sup>\*</sup>

We have prepared the first crystalline and 3D periodically ordered mesoporous quaternary semiconductor photocatalyst in an evaporation-induced self-assembly assisted soft-templating process. Using lab synthesized triblock-terpolymer poly(isoprene-b-styrene-b-ethylene oxide) (ISO) a highly ordered 3D interconnected alternating gyroid morphology was achieved exhibiting near and long-range order, as evidenced by small angle X-ray scattering (SAXS) and electron microscopy (TEM/SEM). Moreover, we reveal the formation process on the phase-pure construction of the material's pore-walls with its high crystallinity, which proceeds along a highly stable  $W^{5+}$  compound, by both *in situ* and *ex situ* analyses, including X-ray powder diffraction (XRPD), Fourier transform infrared spectroscopy (FTIR) and electron paramagnetic resonance (EPR). The resulting photocatalyst CsTaWO<sub>6</sub> with its optimum balance between surface area and ordered mesoporosity ultimately shows superior hydrogen evolution rates over its non-ordered reference in photocatalytic hydrogen production. This work will help to advance new self-assembly preparation pathways towards multi-element multifunctional compounds for different applications, including improved battery and sensor electrode materials.

Received 12th December 2017, Accepted 17th January 2018 DOI: 10.1039/c7nr09251b

rsc.li/nanoscale

## Introduction

Heterogeneous photocatalysis is considered a promising method to convert and store solar energy by deriving chemical fuels, *e.g. via* water splitting into hydrogen and oxygen.<sup>1-6</sup> However, photocatalytic efficiencies are strongly limited by charge carrier recombination at lattice defects, grain boundaries, or at the surface of the semiconductor.<sup>7</sup>

Improvements in activity of the most prominent semiconductors, which are mainly binary compounds including  $TiO_2$ ,  $WO_3$ ,  $\alpha$ -Fe<sub>2</sub>O<sub>3</sub>, or CdS, are severely hampered by their intrinsic material limitations such as low light absorption,

In order to enhance photocatalytic activity, increasing surface area has been investigated by preparing complex nanoporous semiconductors, including mesoporous materials with pore sizes between 2 and 50 nm. Simply increasing the surface area is often not enough to improve activity in photocatalysis, as other parameters like pore size, pore morphology, and pore surface faceting play a crucial role in optimizing performance. In contrast to binary compounds, it remains highly challenging to prepare phase-pure mesoporous ternary/quaternary oxides with well-defined and ordered porosity. The complex hydrolysis and condensation kinetics of multiple precursors need to be controlled, requiring fine-tuning of reaction

insufficient charge carrier mobility, inappropriate band positions, and high toxicity. Therefore, the need for new and efficient photocatalysts by expanding the materials library is evident, and a number of more complex ternary and quaternary semiconductors have been found to be very active candidates.<sup>8–10</sup> In contrast to binary compounds, ternary and quaternary oxides allow the exchange of two and three different cations, respectively, while keeping the same crystal structure, thus providing more flexibility to tailor and control properties such as band gap, band positions, and trap states.<sup>11</sup>

<sup>&</sup>lt;sup>a</sup>Institute of Physical Chemistry, Justus-Liebig-University Giessen, Giessen, Germany. E-mail: roland.marschall@phys.chemie.uni-giessen.de

<sup>&</sup>lt;sup>b</sup>Institut für Materialchemie, Technische Universität Wien, Vienna, Austria <sup>c</sup>INM – Leibniz Institute for New Materials, Campus D2 2, 66123 Saarbrücken, Germany

<sup>&</sup>lt;sup>d</sup>Department of Materials Science and Engineering, Saarland University, Campus D2 2, 66123 Saarbrücken, Germany

<sup>&</sup>lt;sup>e</sup>Materials Science & Engineering, Cornell University, Ithaca, NY 14853, USA

 $<sup>\</sup>dagger$  Electronic supplementary information (ESI) available: Two-dimensional SAXS datasets, additional SEM image, XRPD pattern of the product of  $Cs_2CO_3$  plus  $TaCl_5$  dissolved in EtOH and dried at 80 °C, in situ XRPD patterns of the dried ISO-Cs\_2WOCl\_5 composite, TG-MS data and product traces. See DOI: 10.1039/c7nr09251b

conditions and interactions between different precursors, as well as their diverse solubility and sol–gel transition behavior. Moreover, crystallization and crystallite growth need to be tailored in localized nanosized environments to avoid pore structure collapse.

Therefore, the choice of template or structure-directing agent enabling a three-dimensionally (3D) accessible pore network, such as gyroidal structures, <sup>15</sup> with large ordered and interconnected pores is crucial for the final application. The structure-directing agent must not disturb the crystallization process and needs to be removed without pore collapse, preferably at temperatures exceeding those used for the initial network crystallization, which is hardly possible with *e.g.* Pluronic P123 due to its low decomposition temperature. <sup>16</sup> If not fully controlled, formation of undesired by-phases, phase separation, or simply a less porous or even non-porous material due to ripening processes or phase transformations during processing can be the result.

These are indeed major challenges; yet once solved, ordered mesoporous quaternary semiconductors have the potential to open up a route towards a new, highly customizable generation of photocatalysts, providing tunable pore morphology and accessibility to avoid mass transport limitations, and adjustable response by tailored surface properties.

CsTaWO<sub>6</sub> is a well-understood semiconductor and fulfills the major criteria for sufficient light induced hydrogen generation. The position of the conduction band minimum at -0.5 eV vs. NHE is perfectly suited for the generation of hydrogen, including sufficient overpotential.<sup>11</sup> This compound has further been reported as an active photocatalyst for water splitting with a band gap of 3.6 eV, 17 which can be decreased by nitrogen and/or sulfur doping down to 2.4/2.1 eV resulting in visible light activity. 18,19 It has been prepared in the past via a solid state reaction, <sup>17</sup> sol-gel synthesis, <sup>20</sup> as nanoparticles *via* hydrothermal synthesis.<sup>21</sup> Moreover, CsTaWO<sub>6</sub> is highly crystalline irrespective of its nanostructure and crystallizes in a single crystal phase, the cubic defect-pyrochlore structure. The latter is a considerable advantage over materials like TiO2 as no phase transformation occurs during temperature treatments, that could lead to structure collapse, e.g. on the way to the final mesoporous material.

Here we successfully employ a tailor-made triblock-terpolymer poly(isoprene-b-styrene-b-ethylene oxide) (PI-b-PS-b-PEO, or simply ISO), used in the past to structure-direct binary oxides, <sup>14,22</sup> to prepare a 3D periodically ordered mesoporous quaternary semiconductor, CsTaWO<sub>6</sub>, for photocatalytic hydrogen production. We reveal details of its complex formation mechanism in controlling the hydrolysis and condensation reaction of three metal precursors simultaneously, thereby highlighting design rules that will help to synthesize other multi-element and multifunctional porous materials using facile and cost-effective self-assembly approaches as opposed to more complex chemical/physical vapor deposition or molecular beam epitaxy techniques.

## Experimental

#### **Materials**

Benzene (99%, TCI America), 1,1-Diphenylethylene (DPE, 98%, Alfa Aesar), isoprene (99%, <1000 ppm p-tert-butylcatechol, Sigma Aldrich), sec-Butyllithium (secBuLi, 1.4 M in cyclohexane, Sigma Aldrich), n-butyllithium (1.6 M in hexane, Acros Organics), styrene (ReagentPlus©, stabilized, Sigma Aldrich), calcium hydride (CaH2, 1-20 mm granules, 88-98%, Alfa Aesar), ethylene oxide (EO, 99.8%, Sigma Aldrich), potassium (98%, pieces in mineral oil, Fisher Scientific), hydrochloric acid (HCl, reagent grade, 37%, Sigma Aldrich), methanol (99%, Macron), naphthalene (99%, Fisher Scientific), tetrahydrofuran (THF, 99%, <1000 ppm stabilizer, Fisher Scientific) and chloroform (CHCl<sub>3</sub>, 99.8+%, ACS, Fisher Scientific), cesium carbonate (99.9%, Alfa Aesar), tantalum chloride (99%, H. C. Starck) and tungsten chloride (99%, H. C. Starck) were either purified as described or if not further described used as received.

#### **Syntheses**

Poly(isoprene-block-styrene-block-ethylene oxide) (ISO; PI-b-PSb-PEO) terpolymer was synthesized via living sequential anionic polymerization as described elsewhere. 23,24 Briefly, all chemicals were distilled from either nBuLi or CaH2 to remove all residual impurities, water, and dissolved gases. The first two blocks were sequential synthesized in benzene using sec-BuLi as initiator. The living PI-b-PS was endcapped with double-distilled EO and terminated with MeOH/HCl. To exchange the lithium counter ion with potassium, the polymer was washed several times with deionized water (18.2  $M\Omega$ ), thoroughly dried, dissolved in THF and (re-)initiated by potassium naphthalenide. An appropriate amount of double-distilled EO was added and the living ISO was then terminated by MeOH/HCl, dried and dissolved in CHCl<sub>3</sub>. The polymer/CHCl<sub>3</sub> solution was washed several times with deionized water and finally precipitated in an aliquot of MeOH, filtrated, dried and stored at −20 °C to prevent cross-linking or degradation.

In a typical synthesis for mesoporous CsTaWO $_6$ , 66 mg Cs $_2$ CO $_3$  was dissolved in 2 mL abs. EtOH, and stirred for one hour. Then, 145 mg TaCl $_5$  were added, with one hour of additional stirring, followed by the addition of 158 mg WCl $_6$  and another hour of stirring. In a second vessel, 405 mg ISO-polymer was dissolved in 11.55 g THF. 2 mL of polymer solution and 250  $\mu$ L of precursor solution were combined in six glass vessels, and stirred for another 2 hours. The solutions were then transferred into 5 mL PTFE cups, followed by solvent evaporation under a glass dome at 40 °C on a heating plate for two days. Afterwards, another drying step at 50 °C in a vacuum furnace was performed. The resulting residue was calcined for 1 hour at 550 °C (heating rate: 1 °C min $^{-1}$ ).

#### Characterization

To determine polydispersity and molar mass of the synthesized ISO terpolymer, gel permeation chromatography (GPC) was used with polyisoprene standards (Polymer

Nanoscale Paper

Table 1 Structural data of used ISO polymer

Name	$M_{\rm n} ({\rm g \ mol}^{-1})$	PDI	$f_{\mathrm{PI}}^{}a}\left(\% ight)$	$f_{\mathrm{PS}}^{a}\left(\%\right)$
ISO006	$80400\left(\mathrm{NMR}^{b}\right)$	1.09	28.9 (1.4) 2.3 (3.4)	64.2

<sup>&</sup>lt;sup>a</sup> From NMR. <sup>b</sup> Calculated from a combination of integrated <sup>1</sup>H-NMR spectra and GPC data of the PI block using PI standards for calibration.

Standards Service, Mainz, Germany). Polymeric samples were dissolved in THF (1 mg mL<sup>-1</sup>) and filtered through a 0.45 µm PTFE filter. GPC measurements were performed on a Waters ambient-temperature GPC system equipped with a Waters 2410 differential refractive index (RI) detector.

<sup>1</sup>H-Nuclear magnetic resonance spectroscopy (<sup>1</sup>H-NMR) was used to analyze the composition of the triblock-terpoylmer. A Bruker Avance III HD Nanobay equipped with a SampleXpress autosampler and a BBFO probe for 5 mm tubes was used. Samples were dissolved in CDCl3 and measured at 300 MHz (Table 1).

X-ray powder diffraction (XRPD) patterns were measured on an X'Pert PRO diffractometer from PANalytical Instruments (Cu Kα radiation,  $\lambda = 1.5418 \text{ Å}$ ) with an acceleration voltage of 40 kV and an emission current of 40 mA. Data were recorded in a step scan mode from 10-90° with a step size of 0.03°. For Rietveld refinement a FULLPROF 2.05 software and a modified Thompson-Cox-Hastings Pseudo-Voigt profile function was used. The quality of the fits was characterized through the weighted profile R-factor  $(R_{wp})$  and the goodness of fit  $(\chi^2)$ . In situ XRPD measurements were performed on an X'Pert PRO MPD diffractometer from PANalytical Instruments (also Cu Ka radiation) equipped with an HTK 1200 chamber from Anton Parr.

Scanning electron microscopy (SEM) was performed on a Zeiss Merlin instrument. High resolution transmission electron microscopy (HRTEM) images were obtained on a FEI Tecnai F20 operated at 200 kV. The powdered oxide sample was briefly sonicated in EtOH and the solution was dropped onto a carbon coated Cu grid.

Nitrogen physisorption experiments at 77 K were acquired with an Autosorb IQ2 automated gas adsorption station from Quantachrome Corporation. Prior to the measurement, samples were degassed in vacuum at 120 °C overnight. For elucidation of the specific surface area, the Brunauer-Emmett-Teller (BET) model was used. NLDFT was used to determine the pore diameter.

Fourier transform infrared (FTIR) spectra were recorded on a Bruker Optics Alpha instrument in a range of 400 to 4000 cm<sup>-1</sup> with a resolution of 4 cm<sup>-1</sup>, using a pellet consisting of KBr and the verified sample.

Electron paramagnetic resonance (EPR) spectra were measured on a 9.5 GHz EPR spectrometer Bruker ESP 300E (10 mW power, modulation amplitude 1 G, modulation frequency 100 kHz). The EPR setup was equipped with an Oxford-He-flow cryosystem. The measurement temperature was set to 100 K to obtain optimum signal to noise ratio.

SAXS measurements were performed at station G1 of the Cornell High Energy Synchrotron Source (CHESS) with a beam energy of 9.83 keV and a sample-to-detector distance of 2 m. A DECTRIS Eiger 1 M pixel array detector was used to collect the two-dimensional scattering data, which were integrated to produce intensity vs. q data plots using the Nika package for Igor Pro.<sup>25</sup> Intensity was normalized by the exposure time and incident beam intensity.

### Photocatalytic hydrogen evolution

300 mg photocatalyst were suspended in 600 mL of an aqueous methanol solution (10 vol%) and filled into a homemade inner irradiation-type quartz reactor. 26 A 700 W Hg midpressure immersion lamp set to 50% (350 W, Peschl UV-Consulting) was used as light source and cooled to 10 °C with a double-walled quartz mantle using a thermostat (LAUDA RP845). Gas evolution was measured online using a mass spectrometer (Hiden HPR-20 Q/C). Argon 5.0 was used as carrier gas; the continuous gas flow was controlled by Bronkhorst mass flow controller. The gas flow was set to 100 NmL min<sup>-1</sup>. All reactions were performed at 10 °C. Before photocatalytic reactions were initiated, the whole system, with the photocatalyst included, was flushed with Argon 5.0 for one hour to remove any trace of air. Successive co-catalyst precursor (Na<sub>3</sub>RhCl<sub>6</sub> (Aldrich)) addition for photodeposition was performed through a rubber sealing (without opening the reactor) after turning off the light source to avoid prolonged intermediate Argon flushing for air removal.

## Results and discussion

## Materials synthesis and characterization

Polystyrene-block containing copolymers have been used quite often in the past to prepare ordered mesoporous metal oxides like WO<sub>3</sub>,<sup>27</sup> Ta<sub>2</sub>O<sub>5</sub>,<sup>28</sup> TiO<sub>2</sub>-SiO<sub>2</sub>-composite films,<sup>29</sup> and even mesoporous metals.<sup>30</sup> Using ISO as structure directing agent a variety of different mesoporous (>20 nm) morphologies are accessible, such as hexagonally-packed cylinders (HEX), double gyroid (GD) and the alternating gyroid (GA), recently reported for carbon, TiO2 and Ta2O5, respectively. 14,22,31 Besides selective chemical compatibility of the O block with inorganic precursors, tailoring of final pore size by variation of either block sizes or overall terpolymer molar mass, renders this system attractive when compared to alternative templating methods.

ISO terpolymer was optimized as structure-directing agent in its composition and overall molar mass to yield large pore 3D periodically ordered mesoporous CsTaWO<sub>6</sub>. The desired terpolymer was synthesized employing sequential living anionic polymerization to produce well-defined composition (PI: PS: PEO vol% = 31:64:5), low polydispersity index (PDI) of 1.09, and average molar mass,  $M_{\rm n}$ , of 80k (see Experimental section). The polymer was dissolved in THF and combined with a defined aliquot of a solution containing the metal precursors in EtOH (see Experimental section). The mixture was

then transferred into PTFE dishes and placed on a hotplate for evaporation induced self-assembly (EISA). Samples with well-defined G<sup>A</sup> morphology were obtained from slow solvent evaporation in a saturated solvent vapor environment. To remove the residual solvent after microphase separation and avoid pore collapse, a two-step drying process was applied. Vacuum-assisted drying at 40 °C and 50 °C removes the undesired solvent residues and promotes cross-linking of the embedded precursors, respectively. Further calcination at 550 °C in air simultaneously removes the polymeric structure-directing agent and crystallizes the inorganic material to yield highly ordered mesoporous CsTaWO<sub>6</sub>.

Small angle X-ray scattering (SAXS) was used to investigate the mesoscale structure of our mesoporous CsTaWO<sub>6</sub>. The two-dimensional SAXS datasets (Fig. S1 ESI†) exhibit a remarkable degree of order indicative of mesoporous material with large grains. Fig. 1 shows the corresponding azimuthally integrated one-dimensional SAXS patterns of the mesoporous CsTaWO<sub>6</sub> before and after calcination. The ordered material shows well-defined reflections, consistent with expected reflections for an alternating gyroid (I4<sub>1</sub>32) lattice, <sup>14</sup> as indicated by solid vertical marks. The first main reflection in the SAXS patterns can be used to determine the average cubic lattice constant,  $d_{100}$ . The ordered ISO/CsTaWO<sub>6</sub> hybrid before calcination had a  $d_{100}$  spacing of 85.4 nm, which decreased to 56.7 nm after calcination, consistent with expected structural shrinkage of the polymer-inorganic hybrid system upon heat processing during conversion to CsTaWO<sub>6</sub>.

Fig. 2a and b show SEM images of the resulting powders after calcination depicting a highly and periodically ordered mesoporous morphology observed over a wide area (Fig. S2, ESI†), with mesopores around 40 nm in size as determined

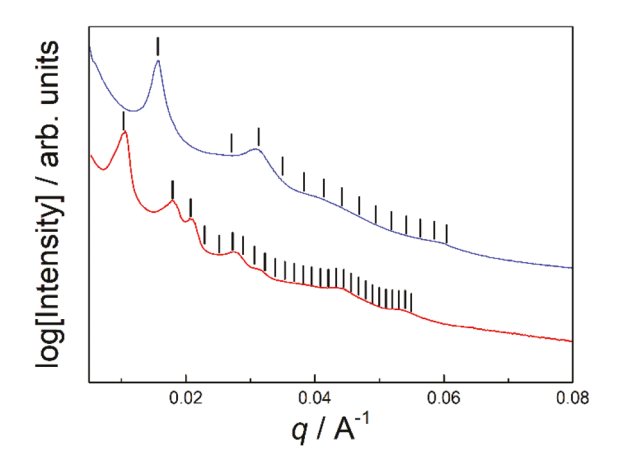


**Fig. 1** SAXS pattern of ordered mesoporous CsTaWO<sub>6</sub> before (red) and after calcination (blue) at 550 °C. The peak markings are for reflections consistent with the cubic alternating gyroid morphology ( $I4_132$ ) with a  $d_{100}$  spacing of 85.4 nm before calcination and 56.7 nm after calcination. These patterns are taken of a selected angular range of 45°  $\pm$  20° for the sample before calcination and 110°  $\pm$  60° for the sample after, in order to capture the intense oriented spots. The blue pattern is shifted vertically for clarity.

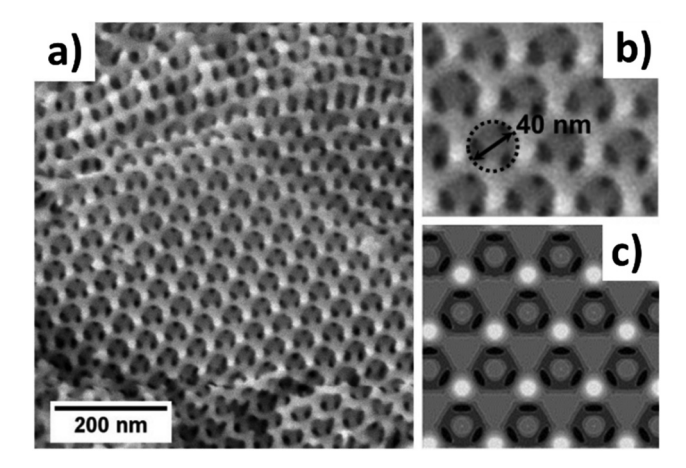


Fig. 2 (a) SEM image of ordered mesoporous CsTaWO<sub>6</sub> calcined at 550 °C; (b) a higher magnification of (a); (c) simulated image of an  $G^A$  pore structure along the [111] direction, corresponding to the observed structure in (a) and (b) (reprinted with permission of ref. 32, © 1998 American Institute of Physics).

from images at higher magnifications. Comparison with a simulated image (Fig. 2c) corroborates the assignment to a gyroidal pore structure. Such large mesopores are beneficial for photocatalytic hydrogen production. <sup>14,33,34</sup>

Furthermore, 3D networked mesopores like the ones shown in Fig. 2 provide easy pore access and reduce pore blocking, ultimately enabling superior photocatalytic performance. TEM images in Fig. 3 corroborate SEM results by also exhibiting a highly ordered and periodic mesoporous morphology of the calcined CsTaWO<sub>6</sub> samples. Together with the SAXS data presented above, all microscopy investigation results are consistent with an alternating gyroid ( $G^A$ ) structure.

Nitrogen physisorption measurements were performed on mesoporous CsTaWO<sub>6</sub> after calcination to investigate porosity and surface area (Fig. 4). Using the Brunauer–Emmet–Teller (BET) model, a surface area of 37 m<sup>2</sup> g<sup>-1</sup> was determined, slightly smaller than what was found for non-ordered mesoporous CsTaWO<sub>6</sub>,  $^{33,34}$  and consistent with a larger mesopore size in the current material.

The isotherm in Fig. 4a shows a typical hysteresis loop at high relative pressures indicating large mesopores. Applying a NLDFT adsorption model for cylindrical pores in SiO<sub>2</sub> onto the adsorption branch of the isotherm (Fig. 4b) provides a very

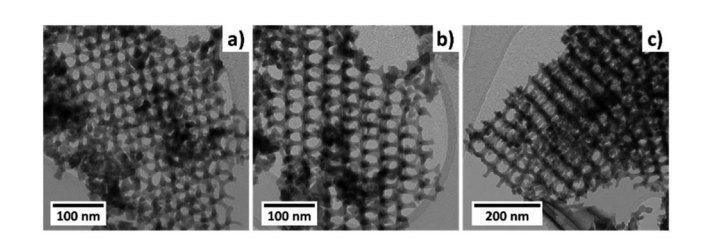


Fig. 3 TEM images of ordered mesoporous CsTaWO $_6$ , calcined at 550 °C.

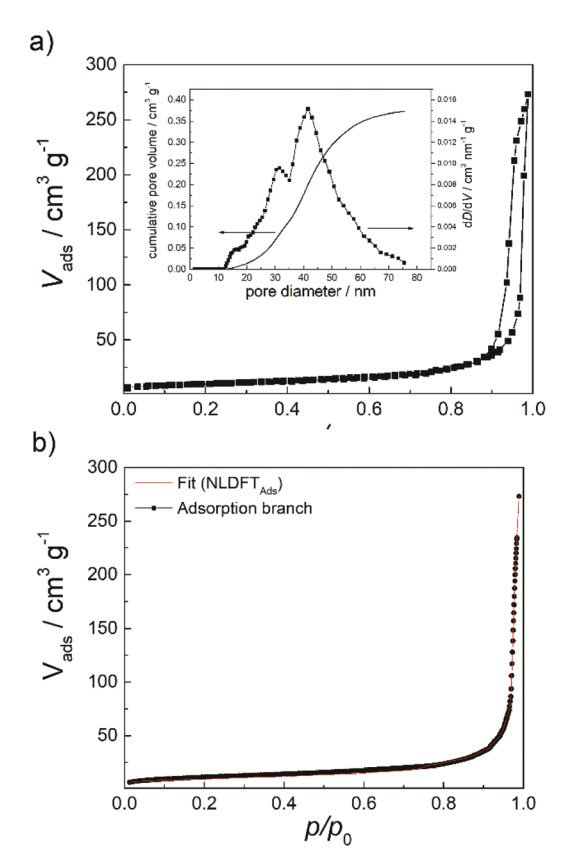


Fig. 4 Nitrogen physisorption measurement results on mesoporous CsTaWO<sub>6</sub>: (a) isotherm of CsTaWO<sub>6</sub>, calcined at 550 °C; inset: respective pore size distribution from NLDFT and cumulative pore volume. (b) Fit of the adsorption branch using the NLDFT model for cylindrical pores in SiO<sub>2</sub>.

accurate fit to the data and leads to a pore size distribution displayed in the inset of Fig. 4a centred at 42 nm, which is in good agreement with the pore dimensions observed with SEM (compare with Fig. 2). Isotherm and pore size distribution are as expected for an ISO-derived mesoporous materials with 3D gyroidal pore structure.14 A small friction of connecting mesopores with a slightly reduced diameter (31 nm) can be seen in the NLDFT pore size distribution calculation, probably due to sample preparation.

X-ray powder diffraction (XRPD) supported by Rietveld refinement was performed on calcined samples to analyze crystal structure and phase purity, both being highly important for photocatalytic performance. Results displayed in Fig. 5 suggest a highly crystalline product after calcination. No impurity phases could be detected in such XRPD patterns, and all reflections could be indexed according to the cubic defect-pyrochlore structure,  $Fd\bar{3}m$ , of CsTaWO<sub>6</sub> (reference: JCPDS 25-0233). The average crystallite size,  $L_a$ , after calcination is 10 nm, as determined via Rietveld refinement. This value is slightly below the optimum crystallite size found for CsTaWO<sub>6</sub> in the form of nanoparticles, <sup>21</sup> but corresponds well with the wall thickness observed in TEM. To the best of our knowledge, this is the first fully crystalline and period-

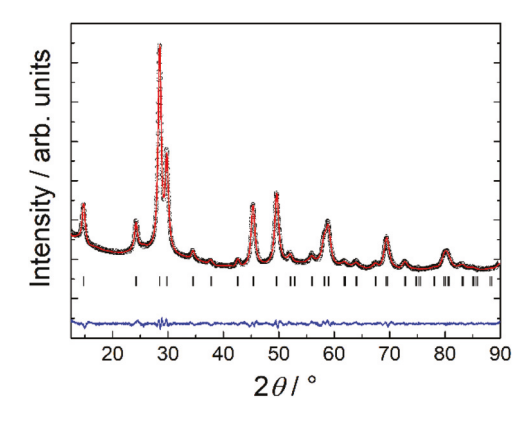


Fig. 5 XRPD pattern of mesoporous CsTaWO<sub>6</sub> with Rietveld refinement. Black symbols mark experimental data, while the red solid line represents the calculated pattern. Individual peak positions and residue plot (blue) between experimental data and the fit are shown below the diffractogram, respectively.

ically ordered mesoporous quaternary semiconductor ever reported.

#### Investigation of the formation mechanism

Ordered mesoporous CsTaWO6 was prepared via a nonaqueous sol-gel route. In order to understand how this phasepure mesoporous CsTaWO6 is formed, we have investigated the formation mechanism in more detail. This investigation is of general interest, in particular outlining a general preparation pathway to synthesize complex multi-element catalysts, tungstates,35 aluminates,36 and other compounds<sup>37–39</sup> with ordered mesoporous morphology.

The first step in synthesizing ISO-derived mesoporous CsTaWO<sub>6</sub> is the preparation of the precursor solution, starting by dissolving Cs2CO3 in ethanol (EtOH) followed by the addition of TaCl<sub>5</sub>. A white powder can be obtained by drying the clear precursor solution at this point, resulting in the XRPD pattern shown in Fig. S3 (ESI†). The reflections belong to the cubic CsCl phase, which indicates the reaction of both precursors, most likely according to the following equation:

$$\begin{aligned} \text{Cs}_2\text{CO}_3 + \text{TaCl}_5 + 2\,\text{C}_2\text{H}_5\text{OH} \rightarrow & 2\,\text{CsCl} + \text{Ta}(\text{OC}_2\text{H}_5)_2\text{Cl}_3 \\ & + \,\text{H}_2\text{CO}_3. \end{aligned} \tag{1}$$

The tantalum ethoxy chloride can further condense to an amorphous tantalum oxide, which may contribute to the strong background in the XRPD pattern between 20 and 35°  $2\theta$ . The formed carbonic acid decomposes into  $CO_2$  and water, released water accelerates further condensation of tantalum chloride/tantalum ethoxychloride (and later of the tungsten chloride).

After adding WCl6 to the clear solution of Cs2CO3 and TaCl<sub>5</sub> in EtOH, the solution immediately turns yellow and gets darker with time, ending up as an orange/brown solution. Due to the high excess of ethanol as solvent for the precursor, WCl<sub>6</sub> hydrolyses in a similar fashion as described by eqn (1), but then further condenses with other molecules of tungsten

chloride or tungsten ethoxy chloride. One example for this condensation is shown in eqn (2):<sup>40</sup>

$$\begin{split} 2\,W(OC_2H_5)_2Cl_3 &\to Cl_2(C_2H_5O)_2W - O - W(OC_2H_5)Cl_3 \\ &\quad + C_2H_5Cl. \end{split} \tag{2}$$

The hydrolysis behavior of WCl $_6$  in EtOH is already known to be dependent on the molar ratio of the two compounds. <sup>40</sup> At a molar ratio of 1:1, W(OC $_2$ H $_5$ OH)Cl $_5$  is formed, but about half of this compound decomposes to WOCl $_4$  and C $_2$ H $_5$ Cl. At higher amounts of EtOH, the reaction proceeds further and the product for a ratio of around 10:1 has an average composition around W(OC $_2$ H $_5$ OH) $_3$ .5Cl $_2$ .5. In our experiments, the molar ratio of EtOH to WCl $_6$  is ~100:1. At such high excess of EtOH, another reaction can occur, forming pentavalent tungsten:

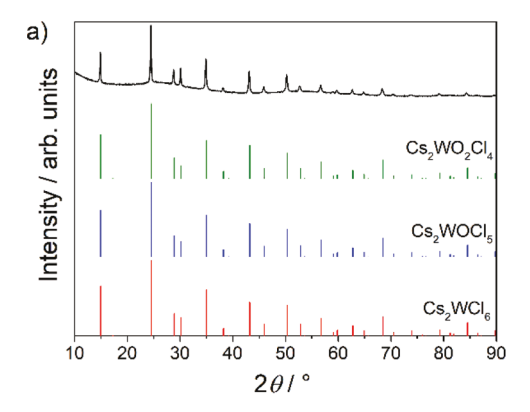
$$WCl_6 + 2 C_2 H_5 OH \rightarrow W(OC_2 H_5)_2 Cl_3 + 2 HCl + \frac{1}{2} Cl_2$$
 (3)

This behavior was confirmed in previous studies *via* elemental analysis and EPR of the reaction solution. <sup>40</sup> It is therefore possible to get stable compounds with pentavalent tungsten in non-aqueous sol–gel processes.

As was described above, the precursor solution has an orange-brownish color, which can be evidence for the presence of WOCl<sub>4</sub>. <sup>44</sup> After drying at 40 °C under high solvent vapor pressure, the solid has a dark red-blue color. The oxidation state of tungsten changes from +VI in WCl<sub>6</sub> to +V after hydrolysis and condensation. This oxidation state can often be observed via strong blue coloration (see inset Fig. 6b). <sup>45</sup> The red color shade originates from the formation of a cesium tungsten (oxy)chloride, which is known to be of red color. <sup>44</sup> An XRPD pattern of the solid after drying is shown in Fig. 6a. All reflections can be attributed to a cubic crystal structure with space group  $Fd\bar{3}m$ .

From XRPD, however, it is not possible to obtain the exact composition of this compound, because  $Cs_2WCl_6$ ,  $Cs_2WOCl_5$ , and  $Cs_2WO_2Cl_4$  do all have the same crystal structure, and the changes in relative intensities of the diffraction peaks are very weak (small changes of the intensities can be seen in the region around  $2\theta \approx 30^\circ$ ), as shown in Fig. 6a.

An indication for the existence of tungsten in the oxidation state +V is the color, as  $Cs_2WOCl_5$  is reported to be a greenblue solid. <sup>46</sup> Due to the different oxidation states of tungsten in the three compounds  $(Cs_2W(+IV)Cl_6, Cs_2W(+V)OCl_5,$  and  $Cs_2W(+VI)O_2Cl_4)$ , we used EPR spectroscopy to unravel the stable composition after drying. In EPR, the only active species is  $W^{5+}$  because of the unpaired d-electron in this oxidation state (electron configuration [Xe]  $4f^{14}$   $5d^1$ ). The EPR spectrum of the dried precursor solution shows two signals in the range between 3500 and 4000 G (black curve, Fig. 6b, arrows). The two signals with  $g_{\parallel}=1.79$  and  $g_{\perp}=1.76$  fit perfectly to the experimentally measured and theoretically calculated values for  $W^{5+}$  in the  $(WOCl_5)^{2-}$  anion. <sup>41,42</sup> These results strongly support the proposed mechanism in eqn (4) and (5). The intermediate product has most probably the composition



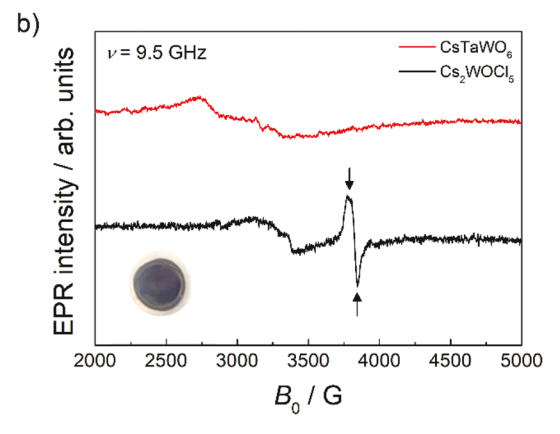


**Fig. 6** XRPD and EPR characterization of dried precursor solution material, (a)  $Cs_2CO_3$ ,  $TaCl_5$  and  $WCl_6$  dissolved in EtOH, after drying. Reference cards of  $Cs_2WCl_6$ ,  $Cs_2WOCl_5$  and  $Cs_2WO_2Cl_4$  are shown below (JCPDS card no. 40-9674, 18-0374, and 22-0202, respectively); (b) EPR spectra of  $Cs_2WOCl_5$  (black), exhibiting the typical EPR signature (see arrows) for  $W^{5+}$  in the  $(WOCl_5)^{2-}$  anion at  $g_{\parallel}=1.79$  and  $g_{\perp}=1.76$ ,  $^{41,42}$  and  $CsTaWO_6$  (red) for which no  $W^{5+}$  signature is found.  $^{43}$ 

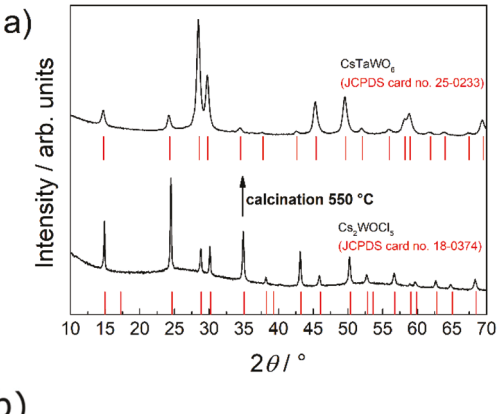
Cs<sub>2</sub>WOCl<sub>5</sub>. It is notable that this W<sup>5+</sup> intermediate is air-stable for several weeks without any observable color change.

However, the targeted compound is CsTaWO<sub>6</sub>. Thus, half of the stoichiometric amount of tungsten and all of the tantalum are missing in this intermediate product.

It has already been mentioned that tantalum could be present in the form of an amorphous tantalum oxide/tantalum oxychloride before the addition of tungsten chloride, which could also be the case after the addition. Furthermore, tantalum could be incorporated in the  $Cs_2WOCl_5$  structure, partially replacing tungsten of the same valence ( $Cs_2TaOCl_5$ ). This would also lead to a very fine mixture of the precursor, which is beneficial for the following calcination step to form the final  $CsTaWO_6$ .

Fig. 7a shows the XRPD patterns of the precursor solution after first drying at 40 °C and subsequent vacuum drying at 50 °C, as well as following calcination at 550 °C. In both cases, a cubic crystal system is observed, but the relative intensities and peak widths of the reflections change considerably. The crystal structures of the oxychloride,  $Cs_2WOCl_5$ , and the defect-pyrochlore,  $CsTaWO_6$ , are illustrated in Fig. 7b. The

Nanoscale



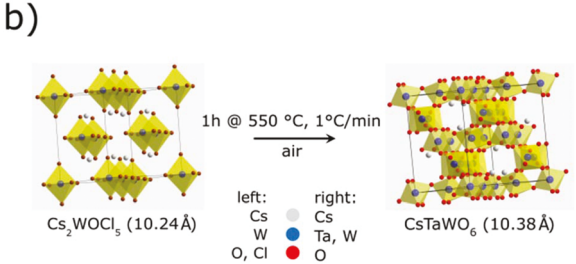


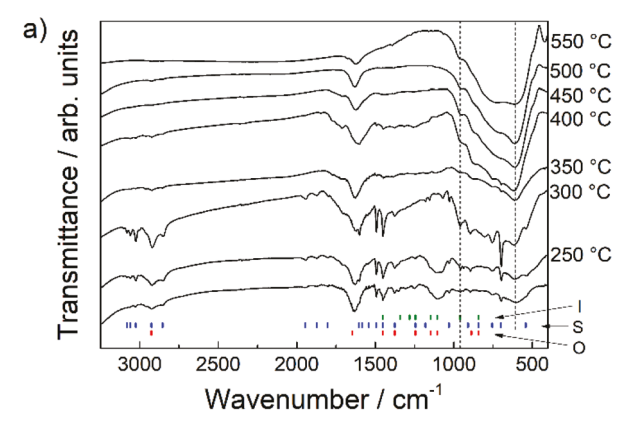
Fig. 7 Comparison of XRPD derived structures of dried precursor solution and calcined materials, (a) XRPD patterns of the dried precursor solution before and after calcination; (b) crystal structures of Cs<sub>2</sub>WOCl<sub>5</sub> (JCPDS card no. 18-0374) and CsTaWO<sub>6</sub> (JCPDS card no. 25-0233). 46

lattice parameters of both compounds are very similar, enabling a smooth transformation via oxidation and Cs<sub>2</sub>WOCl<sub>5</sub> possibly acting as a host crystal. In principle, in both structures the transition metal is six-fold octahedrally coordinated with either chlorine or oxygen. During oxidation, all residual chlorine atoms are replaced by oxygen.

The exact mechanism of the oxidation can be followed by in situ and ex situ XRPD as well as ex situ IR spectroscopy. Ex situ measurements were executed after heating up the dried precursor solution to the respective temperatures (Fig. 8a & b), while in situ XRPD measurements were performed in a high temperature chamber under air with the ground powder (Fig. S4†). Proof for the existence of W-O bonds, either in the Cs<sub>2</sub>WOCl<sub>5</sub> or the amorphous gel, can be found in the IR spectrum of the red-blue solid before calcination, which includes a band at 957 cm<sup>-1</sup> that can be attributed to the stretching mode of W-O in Cs<sub>2</sub>WOCl<sub>5</sub> (Fig. 8a). 47,48

Up to a temperature of 250 °C in the ex situ, and up to a temperature of 150 °C in situ measurements, XRPD patterns (Fig. 8b & S4†) show no changes. The difference in the onset temperature for phase transformation between the two sets of experiments originates from the sample preparation procedure: in the in situ XRPD experiments a ground powder was used with a higher contact surface, as a result the transitions occur at lower temperatures compared to the sample in the ex situ XRPD measurements.

Beginning at 200/300 °C, Cs<sub>2</sub>WOCl<sub>5</sub>, starts to decompose: the intensities of the reflections are getting smaller and reflections of the cubic CsCl phase can be detected in the XRPD pat-



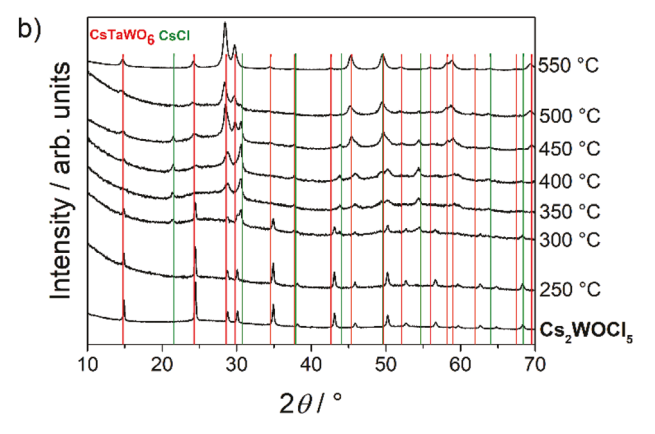


Fig. 8 (a) Ex situ IR spectra of the dried ISO-Cs<sub>2</sub>WOCl<sub>5</sub> composite calcined at different temperatures; (b) ex situ XRPD patterns of the dried ISO-Cs<sub>2</sub>WOCl<sub>5</sub> composite with reference lines for CsCl (green, JCPDS card no. 02-2173) and CsTaWO<sub>6</sub> (red, JCPDS card no. 25-0233), calcined at different temperatures.

terns. At the same time, the IR spectrum does not substantially change and all bands associated with ISO terpolymer are still present. Increasing the temperature to 300/350 °C, reflections of Cs<sub>2</sub>WOCl<sub>5</sub> further disappear, and broad reflections of a cubic structure appear with relative intensities that fit well to the mesoporous CsTaWO<sub>6</sub> compound. An amorphous background in the in situ PXRD patterns can be observed up to 300 °C, indicating tantalum ethoxy chloride and/or amorphous tantalum oxide. IR spectroscopy shows that bands corresponding to the ISO terpolymer start to disappear at 300-350 °C, indicating the decomposition of the structure directing agent, which is corroborated by thermogravimetric analysis in combination with mass spectrometry, TG-MS (Fig. S5 & S6†).

This result is of general importance, indicating that large mesopores using ISO can be obtained and preserved (Fig. 1) when the crystallization process of the final complex compound starts before ISO decomposition. Keeping this in mind, other complex and multi-element compounds could be prepared with 3D periodically ordered mesoporous morphology using ISO as structure-directing agent.

At a temperature of around 500 °C, only weak reflections of CsCl remain (e.g. at around  $2\theta = 30^{\circ}$ , Fig. 8b) and finally disappear only after heating to 550 °C, when pure crystalline CsTaWO<sub>6</sub> is obtained. The final temperature step is needed to dispose of the CsCl, and to get a homogenous distribution of tantalum and tungsten (B and B') on the Wyckoff 16c position, observable as the broad band at 500–1000 cm<sup>-1</sup> in IR spectroscopy (Fig. 8a), which becomes nearly a plateau. This means metal–oxygen bonds are statistically distributed and no accumulation of one species (Ta or W) occurs. The corresponding total release of chlorine during heating to 550 °C can also be detected in TG-MS measurements.

Fig. S5† shows the TG analysis curve for the ISO/CsTaWO<sub>6</sub>hybrid. A small mass loss takes place below 100 °C, likely corresponding to adsorbed water. ISO terpolymer decomposition seems to start slowly beyond 150 °C with a strong maximum at 320 °C and another local maximum at approximately 450 °C. 49 Complete decomposition occurs after a temperature treatment at around 500 °C. In Fig. S6,† MS traces of all arising fragments during the thermal treatment of the ISO/CsTaWO<sub>6</sub>-hybrid are illustrated. Starting at a temperature of 150 °C, small hydrocarbon fragments with a number of carbon atoms from 1 to 3 can be detected, corresponding to the degradation of the polyisoprene and poly (ethylene oxide) block in the ISO triblock-terpolymer.50 Evolution of the expected HCl species takes place at a temperature of around 200 °C with a maximum at 300 °C, arising from the decomposition of Cs2WOCl5. Thus, formation of CsTaWO<sub>6</sub> starts before major decomposition of ISO, which strengthens the complex quaternary inorganic matrix during template removal and results in extraordinary long range order of the mesopore system (Fig. S2†). We envision this process to be crucial for the preparation of other mesoporous complex materials and model systems for accessible and highly ordered mesopores.

At around 320 °C, a few strong MS signals appear and can be assigned to hydrocarbons of the general formula  $C_4H_x$  and  $C_6H_y$ . This temperature region and the corresponding mass-to-charge ratios are typical for the decomposition of polystyrene. For higher calcination temperatures, smaller fragments are dominant but with decreasing intensities up to a temperature of around 500 °C. Shortly before 500 °C is reached, another two maxima can be detected for  $CO_2^+$  and  $C^+$ , both providing a hint for the existence of residual carbon inside the pore walls and its removal at this temperature. Weight loss and removal of organic residues are thus observed at much higher temperatures for this ISO-derived sample compared to P123-derived materials,  $^{33,50}$  which may cause increased stabilization of the pore system.

The described observations can be summarized in the following proposed mechanism: at around 300  $^{\circ}$ C, Cs<sub>2</sub>WOCl<sub>5</sub> and tantalum oxychloride form CsTaWO<sub>6</sub> under the consumption of oxygen in a redox reaction, whereas oxygen is reduced and tungsten and chlorine are oxidized. The excessive cesium forms CsCl and chlorine gets released (or HCl if it further

reacts with hydrogen from the terpolymer, water-hydrolyzed educts, or moisture).

Alternatively, if tantalum is also incorporated as  $Cs_2MOCl_5$  (with M = Ta, W), the following similar reaction can occur:

$$Cs_2TaOCl_5 + Cs_2WOCl_5 + 2 O_2 \rightarrow CsTaWO_6 + 3 CsCl + 3.5 Cl_2$$
(5)

With increasing temperature and reaction time, the CsCl in excess is consumed by residual tantalum and tungsten oxychloride, once again in a redox reaction and under release of chlorine (or HCl):

$$CsCl + (Ta, W)O_yCl_z + \frac{6-y}{2}O_2 \rightarrow CsTaWO_6 + \frac{z+1}{2}Cl_2$$
 (6)

The different steps revealed in the formation of this mesoporous tantalum tungstate will be of general importance for the non-aqueous preparation of other mesoporous transition metal-based materials with multi-element composition.

#### Photocatalytic experiments

Hydrogen production from water/methanol mixture was used as a test reaction to investigate the photocatalytic performance of ISO-derived ordered mesoporous CsTaWO<sub>6</sub> (ISO-CTW). Fig. 9 shows the steady-state hydrogen evolution rates of ISO-CTW after calcination and after *in situ* photodeposition of several minor amounts of co-catalyst rhodium (Rh, for details see Experimental section). For comparison, a P123-derived non-ordered mesoporous CsTaWO<sub>6</sub> control sample (P123-

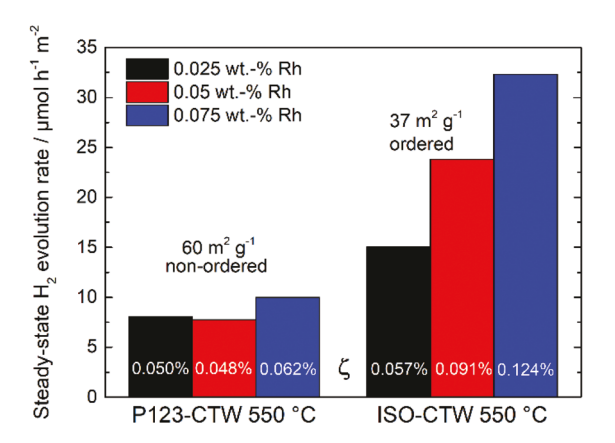


Fig. 9 Steady-state hydrogen evolution rates of ordered *versus* disordered materials. Results for mesoporous ISO-derived CsTaWO $_6$  (ISO-CTW) are compared to non-ordered P123-derived CsTaWO $_6$ , both samples measured in this contribution under identical conditions (described in the Experimental section). Photonic efficiencies ( $\zeta$ ) after actinometry with ferrioxalate are also given.

Nanoscale Paper

CTW) described in ref. 33 was measured in this contribution again at the conditions given in the Experimental section. Even at amounts of Rh deposited as low as 0.025 wt%, the ISO-CTW with alternating gyroid structure already shows a factor two increased activity (relative to the available surface area) as compared to the non-ordered sample. We have to note that the exact amount of Rh and the exact oxidation state of Rh could not be determined due to the low amounts being below the XPS detection limit.

Importantly, increased activity of the ISO-CTW is observed despite its much smaller surface area as compared to the non-ordered sample. Taking the initial surface area of the tested samples into account, the ISO-CTW shows more than 300% hydrogen evolution activity compared to the non-ordered reference (Fig. 9) at Rh loadings as low as 0.075 wt% (the optimum amount for mesoporous P123-CTW<sup>33</sup>) and tested under identical conditions here. The main reason for the strongly increased activity likely lies in the improved transport of liquid educts and gaseous products into and out of the large mesopores, respectively. The median pore diameter of the P123-derived non-ordered mesoporous CsTaWO<sub>6</sub> is only about 10 nm, leading to capillary forces sucking water/methanol into the pores but blocking the release of many product gas bubbles.<sup>33</sup>

In contrast, the large networked mesopores of the ISO-CTW with alternating gyroid pore structure avoid pore blocking, and all gaseous products can be detected. An additional factor could be improved optical effects, *e.g.* multiple light absorption due to the mesoporous structure, <sup>53</sup> which will be investigated in the future.

The results show that even with decreased surface area strong activity enhancements can be achieved when large mesopores are established in semiconductor materials. In the future we want to prepare 3D ordered mesoporous CsTaWO<sub>6</sub> with comparable pore size to P123-CTW, to investigate whether pore ordering (3D deriving from ISO or 2D deriving from P123) actually has an influence on hydrogen evolution, as pore size seems to have as shown before,<sup>33</sup> and to finally demonstrate the detailed relation between mesopore ordering and size with photocatalytic performance.

## Conclusions

In summary, we have prepared the first crystalline and 3D periodically ordered mesoporous quaternary semiconductor, revealed the details of its complex formation mechanism, and used it for photocatalytic hydrogen production. ISO terpolymer-derived ordered mesoporous CsTaWO $_6$  with 3D gyroidal pore structure exhibits mesopores larger than  $42 \pm 10$  nm and a surface area of 37 m $^2$  g $^{-1}$ , which results in superior photocatalytic performance over a non-ordered mesoporous reference material, due to the presence of interconnected large and accessible pores, which cannot be achieved with templates like Pluronic P123. We envision our approach to prepare complex quaternary materials with ordered mesoporous morphology to

have significant influence on synthetic pathways for other complex materials and model systems including *e.g.* perovskites. The chemical interplay between ISO and the inorganic precursors, as revealed in the formation mechanism, will be leading the ways towards a large variety of other multi-element functional mesoporous materials for improved batteries, sensors, and (photo)electrodes.

## Conflicts of interest

There are no conflicts to declare.

# Acknowledgements

We thank Anna-Lena Hansen and Prof. Wolfgang Bensch (both from Christian-Albrechts-University Kiel) for their support with in-situ XRPD measurements. We also thank Jan Philipps, David Specht and Prof. Detlev Hofmann, (1st Physics Institute, JLU Giessen) for EPR measurements and Hubert Woerner (JLU Giessen) for TG-MS measurement. Paul Gebhardt (TU Wien) is acknowledged for additional TEM measurements. T.W. and R.M. gratefully acknowledge funding in the Emmy-Noether program (MA 5392/3-1) of the German Research Foundation DFG. This work made use of the Cornell Center for Materials Research Shared Facilities supported through the NSF MRSEC program (DMR-1120296). This work is further based upon research conducted at the Cornell High Energy Synchrotron Source (CHESS) supported by the National Science Foundation and the National Institutes of Health/ National Institute of General Medical Sciences under NSF award DMR-1332208. P.A.B. was supported by the NSF GRFP program (DGE-1650441). U.B.W. thanks the National Science Foundation for support (DMR-1707836).

## Notes and references

- N. S. Lewis and D. G. Nocera, Proc. Natl. Acad. Sci. U. S. A., 2007, 104, 20142.
- 2 A. J. Bard, J. Am. Chem. Soc., 2010, 132, 7559-7567.
- 3 G. A. Somorjai, H. Frei and J. Y. Park, *J. Am. Chem. Soc.*, 2009, **131**, 16589–16605.
- 4 K. Maeda, M. Higashi, D. Lu, R. Abe and K. Domen, *J. Am. Chem. Soc.*, 2010, **132**, 5858–5868.
- 5 S. Chu, Y. Cui and N. Liu, Nat. Mater., 2017, 16, 16-22.
- 6 J. H. Montoya, L. C. Seitz, P. Chakthranont, A. Vojvodic, T. F. Jaramillo and J. K. Nørskov, *Nat. Mater.*, 2017, 16, 70–81.
- 7 H. Kisch, Angew. Chem., Int. Ed., 2013, 52, 812-847.
- 8 A. Kudo and Y. Miseki, Chem. Soc. Rev., 2009, 38, 253-278.
- 9 F. E. Osterloh, *Chem. Mater.*, 2008, **20**, 35–54.
- 10 X. Chen, S. Shen, L. Guo and S. S. Mao, *Chem. Rev.*, 2010, 110, 6503–6570.
- 11 L. Schwertmann, A. Grünert, A. Pougin, C. Sun, M. Wark and R. Marschall, *Adv. Funct. Mater.*, 2015, 25, 905–912.

**Paper** 

- 12 T. W. Kim and K.-S. Choi, Science, 2014, 343, 990-994.
- 13 M. Thommes, K. Kaneko, A. V. Neimark, J. P. Olivier, F. Rodriguez-Reinoso, J. Rouquerol and K. S. W. Sing, Pure Appl. Chem., 2015, 87, 1051-1069.
- 14 A. S. Cherevan, S. Robbins, D. Dieterle, P. Gebhardt, U. Wiesner and D. Eder, Nanoscale, 2016, 8, 16694-16701.
- 15 M. C. Orilall and U. Wiesner, Chem. Soc. Rev., 2011, 40, 520-535.
- 16 A. Kuschel and S. Polarz, Adv. Funct. Mater., 2008, 18, 1272-1280.
- 17 S. Ikeda, T. Itani, K. Nango and M. Matsumura, Catal. Lett., 2004, 98, 229-233.
- 18 A. Mukherji, R. Marschall, A. Tanksale, C. Sun, S. C. Smith, G. Q. Lu and L. Wang, Adv. Funct. Mater., 2011, 21, 126-132.
- 19 R. Marschall, A. Mukherji, A. Tanksale, C. Sun, S. C. Smith, L. Wang and G. Q. (Max) Lu, J. Mater. Chem., 2011, 21, 8871-8879.
- 20 L. Schwertmann, M. Wark and R. Marschall, RSC Adv., 2013, 3, 18908.
- 21 T. Weller, L. Specht and R. Marschall, Nano Energy, 2017, 31, 551-559.
- 22 M. Stefik, S. Wang, R. Hovden, H. Sai, M. W. Tate, D. A. Muller, U. Steiner, S. M. Gruner and U. Wiesner, J. Mater. Chem., 2012, 22, 1078-1087.
- 23 M. A. Hillmyer and F. S. Bates, Macromolecules, 1996, 9297, 6994-7002.
- 24 J. Chatterjee, S. Jain and F. S. Bates, Macromolecules, 2007, 40, 2882-2896.
- 25 J. Ilavsky, J. Appl. Crystallogr., 2012, 45, 324-328.
- 26 N. Kulischow, C. Ladasiu and R. Marschall, Catal. Today, 2017, 287, 65-69.
- 27 Y. Li, W. Luo, N. Qin, J. Dong, J. Wei, W. Li, S. Feng, J. Chen, J. Xu, A. A. Elzatahry, M. H. Es-Saheb, Y. Deng and D. Zhao, Angew. Chem., Int. Ed., 2014, 53, 9035-9040.
- 28 B. P. Bastakoti, S. Ishihara, S.-Y. Leo, K. Ariga, K. C. W. Wu and Y. Yamauchi, Langmuir, 2014, 30, 651-659.
- 29 Y. Li, B. P. Bastakoti, M. Imura, S. M. Hwang, Z. Sun, J. H. Kim, S. X. Dou and Y. Yamauchi, Chem. - Eur. J., 2014, 20, 6027-6032.
- 30 Y. Li, B. P. Bastakoti, V. Malgras, C. Li, J. Tang, J. H. Kim and Y. Yamauchi, Angew. Chem., Int. Ed., 2015, 54, 11073-11077.
- 31 J. G. Werner, T. N. Hoheisel and U. Wiesner, ACS Nano, 2014, 8, 731-743.

- 32 M. W. Matsen, J. Chem. Phys., 1998, 108, 785-796.
- 33 T. Weller, J. Sann and R. Marschall, Adv. Energy Mater., 2016, 6, 1600208.
- 34 M. Weiss, S. Waitz, R. Ellinghaus, T. Weller and R. Marschall, RSC Adv., 2016, 6, 79037-79042.
- 35 C. M. Blumenfeld, M. Lau, H. B. Grav and A. M. Müller, ChemPhysChem, 2017, 18, 1091-1100.
- 36 J. Y. C. Chen, J. T. Miller, J. B. Gerken and S. S. Stahl, Energy Environ. Sci., 2014, 7, 1382.
- 37 N. Tsvetkov, Q. Lu, L. Sun, E. J. Crumlin and B. Yildiz, Nat. Mater., 2016, 15, 1010-1016.
- 38 B. Han, K. A. Stoerzinger, V. Tileli, A. D. Gamalski, E. A. Stach and Y. Shao-Horn, Nat. Mater., 2016, 16, 121-
- 39 G. M. Rupp, A. K. Opitz, A. Nenning, A. Limbeck and J. Fleig, Nat. Mater., 2017, 16, 640-645.
- Khodzhemirov, V. A. Yevdokimova V. M. Cherednichenko, Polym. Sci. U.S.S.R., 1976, 18, 581-
- 41 H. Kon and N. E. Sharpless, J. Phys. Chem., 1966, 70, 105-111.
- 42 P. Hrobárik, O. L. Malkina, V. G. Malkin and M. Kaupp, Chem. Phys., 2009, 356, 229-235.
- 43 D. Hollmann, O. Merka, L. Schwertmann, R. Marschall, M. Wark and A. Brückner, Top. Catal., 2015, 58, 769-775.
- 44 V. C. Gibson, T. P. Kee and A. Shaw, Polyhedron, 1988, 7,
- 45 O. O. Collenberg, Z. Anorg. Allg. Chem., 1918, 102, 247–276.
- 46 D. Brown, J. Chem. Soc., 1964, 4944-4948.
- 47 A. Sabatini and I. Bertini, *Inorg. Chem.*, 1966, 5, 204–206.
- 48 A. Takase and K. Miyakawa, Jpn. J. Appl. Phys., 1991, 30, L1508-L1511.
- 49 K. W. Tan, H. Sai, S. W. Robbins, J. G. Werner, T. N. Hoheisel, S. A. Hesse, P. A. Beaucage, F. J. DiSalvo, S. M. Gruner, M. Murtagh and U. Wiesner, RSC Adv., 2015, 5, 49287-49294.
- 50 S. Han, C. Kim and D. Kwon, Polymer, 1997, 38, 317-323.
- 51 P. Pfäffli, A. Zitting and H. Vainio, Scand. J. Work, Environ. Health, 1978, 4, 22-27.
- 52 J. L. Gurman, L. Baier and B. C. Levin, Fire Mater., 1987, 11, 109-130.
- 53 B. Fang, A. Bonakdarpour, K. Reilly, Y. Xing, F. Taghipour and D. P. Wilkinson, ACS Appl. Mater. Interfaces, 2014, 6, 15488-15498.